

Transport of flexible chiral objects in a uniform shear flow

Peter Talkner, Gert-Ludwig Ingold, Peter Hänggi

Angaben zur Veröffentlichung / Publication details:

Talkner, Peter, Gert-Ludwig Ingold, and Peter Hänggi. 2012. "Transport of flexible chiral objects in a uniform shear flow." *New Journal of Physics* 14: 073006.
<https://doi.org/10.1088/1367-2630/14/7/073006>.

PAPER

Transport of flexible chiral objects in a uniform shear flow

To cite this article: Peter Talkner *et al* 2012 *New J. Phys.* **14** 073006

View the [article online](#) for updates and enhancements.

Related content

- [Micro-capsules in shear flow](#)
R Finken, S Kessler and U Seifert
- [Mesoscale hydrodynamics simulations of attractive rod-like colloids in shear flow](#)
M Ripoll, R G Winkler, K Mussawisade *et al.*
- [Dynamical properties of granular rotors](#)
Bart Cleuren and Ralf Eichhorn

Recent citations

- [Rheotaxis facilitates upstream navigation of mammalian sperm cells](#)
V. Kantsler *et al*
- [Separation of chiral colloidal particles in a helical flow field](#)
Maria Aristov *et al*
- [Flipping, scooping, and spinning: Drift of rigid curved nonchiral fibers in simple shear flow](#)
Jianghui Wang *et al*

Transport of flexible chiral objects in a uniform shear flow

Peter Talkner¹, Gert-Ludwig Ingold and Peter Hänggi

Institut für Physik, Universität Augsburg, Universitätsstraße 1,

D-86135 Augsburg, Germany

E-mail: peter.talkner@physik.uni-augsburg.de

New Journal of Physics **14** (2012) 073006 (23pp)

Received 13 February 2012

Published 3 July 2012

Online at <http://www.njp.org/>

doi:10.1088/1367-2630/14/7/073006

Abstract. The transport of slightly deformable chiral objects in a uniform shear flow is investigated. Depending on the equilibrium configuration one finds up to four different asymptotic states that can be distinguished by lateral drift velocity of their center of mass, rotational motion about the center of mass and deformations of the object. These deformations influence the magnitudes of the principal axes of the second moment tensor of the considered object and also modify a scalar index characterizing its chirality. Moreover, the deformations induced by the shear flow are essential for the phenomenon of dynamical symmetry breaking: objects that are achiral under equilibrium conditions may dynamically acquire chirality and consequently experience a drift in the lateral direction.

¹ Author to whom any correspondence should be addressed.

Contents

1. Introduction	2
2. The model	3
2.1. Spiral objects and the equation of motion	3
2.2. Characteristics of the mechanical state of an object	6
3. Results	9
3.1. Center of mass motion	11
3.2. Rotational motion	11
3.3. Internal motion and dynamical symmetry breaking	13
4. Role of hydrodynamic interactions	17
5. Conclusions	21
Acknowledgments	22
Appendix. Achiral configurations	22
References	23

1. Introduction

The idea of achieving enantiomer separation on the basis of specific transport properties of chiral objects in flowing fluids [1–3] is very attractive because it opens the way to tackle this also industrially relevant task by purely physical means without the need for specific chemical agents.

Howard *et al* [4] were the first to suggest the use of transport properties of asymmetric objects to separate differently crystallized enantiomers. Later, de Gennes [5] discussed a mechanical way of separating chiral crystals. Only recently, a lateral drift of screw-like objects in shear flows predicted by Brenner [6] was experimentally demonstrated for bodies with a linear extension of the order of centimeters [7], millimeters [8] and micrometers [9]. The direction of this drift, resulting from the coupling of the rotational and translational motions of a chiral object in a fluid, differs for objects with opposite chirality. The mutual interactions between flowing fluids and immersed chiral objects have recently been the subject of various experimental studies. The generation of flow patterns by actively rotating chiral objects was investigated in [10]. The control of actively moving nano-structured propellers was studied in [11]. In [12], the formation of chiral assemblies made of achiral components in a vortex flow is described.

Theoretical studies on the influence of the chirality of a macroscopic object on its transport properties were conducted for sedimentation [13] and for shear flows [14]. Chiral planar three-atomic molecules were studied in clover leaf vortex flows [1] and in flows in channels of various geometries [15, 16]. In these two-dimensional (2D) studies, fluctuating forces were taken into account in order to model the action of thermal fluctuations exerted on the molecules by the surrounding fluid. All studies [1, 13–16], however, are restricted to rigid objects.

Watari and Larson [17] considered 3D, four-atomic molecules that, in equilibrium, assume the form of a regular tetrahedron, which as such is achiral with respect to geometry. When put into a shear flow these molecules are distorted in an asymmetric way owing to

differently deformable bonds between the atoms. As a consequence these molecules experience a lateral drift.

In this work, we study the motion of objects consisting of four mutually interacting spheres with *different* equilibrium bond lengths but identical bond strengths, see equation (2), being suspended in a uniform shear flow. The main mechanisms leading to a lateral drift of the objects, i.e. to a motion perpendicular to the flow direction and to the direction in which the flow speed changes, can be summarized as follows. The shear field of the flow leads to a rotation of the object, which then, like a small propeller, moves in, or opposite to, the direction of the vorticity of the flow. We demonstrate that the rotation is essentially determined by the advection of the spheres with the fluid motion and only slightly influenced by hydrodynamic interactions between the spheres. In a uniform shear flow, coupling between rotational and translational motions, however, is only possible due to hydrodynamic interactions between the spheres.

The direction of the lateral drift is difficult to predict, as is also the case for molecular motors [2]. In general, it depends on all the parameters of the system and also on the initial conditions with which the object is started. These initial conditions may belong to different domains of attraction, eventually leading to different attractors, which may display different forms of rotation of the object and consequently different drift behavior, even with opposite signs.

Due to the deformability of the considered objects, chiral attractors may exist for objects with achiral equilibrium configurations and consequently achiral objects may experience a lateral drift displaying dynamical symmetry breaking. The lateral drift, however, vanishes on average, because for an object with achiral equilibrium configuration chiral attractors can only come in mutually mirror symmetric pairs.

This paper is organized as follows. In section 2, we introduce a class of ‘spiral’ objects, the geometry of which is described by only three parameters, and we specify their equations of motion in terms of bond strengths and hydrodynamic interactions. Further, we introduce the most important quantities needed for the analysis of numerical solutions to the equations of motion (section 2.2). In section 3, we present the results on the center of mass motion (section 3.1), the rotational motion (section 3.2) and the internal motion (section 3.3) with particular emphasis on the dynamical symmetry breaking (section 3.3.1). The role of hydrodynamic interactions is discussed in section 4. The paper closes with a summary and an outlook in section 5.

2. The model

2.1. Spiral objects and the equation of motion

In the present case study, we consider objects consisting of four identical spheres of radius a . The equilibrium configuration of a free object, i.e. a stable configuration with balanced bonding forces between the spheres, is assumed to be of helical form. This form is constructed by positioning the centers of the spheres on a cylinder mantle of radius ρ . Given the location of the first sphere \mathbf{R}_1 , the next one, \mathbf{R}_2 , is found upon rotation by an angle φ about the cylinder axis combined with a translation by h parallel to the cylinder axis, and so on with the third and fourth spheres yielding the respective positions \mathbf{R}_3 and \mathbf{R}_4 , as illustrated by figure 1(a). Hence, if the cylinder axis coincides with the z -direction of a coordinate system and the first sphere

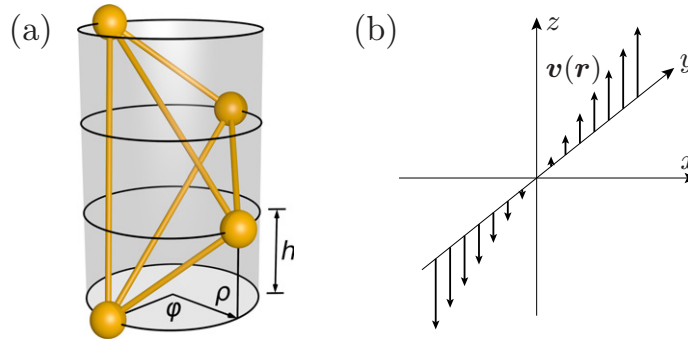


Figure 1. (a) The configuration of a spiral object consisting of four spheres of radius a positioned on a cylinder mantel of radius ρ . Positions of neighboring spheres are distinguished by screw angle φ and rise h . (b) Uniform shear flow: the velocity is independent of x , points in the z -direction and varies in magnitude proportionally to y .

lies in the x -axis of the coordinate system, then the following vectors point to the centers of the spheres sitting on a spiral:

$$\mathbf{R}_n = \rho \mathbf{e}_x \cos[(n-1)\varphi] + \rho \mathbf{e}_y \sin[(n-1)\varphi] + h(n-1)\mathbf{e}_z, \quad n = 1, 2, 3, 4. \quad (1)$$

We model the bonding forces between the spheres of such a ‘spiral’ object by nonlinear, so-called FENE-Fraenkel (finitely extensible nonlinear elastic) springs [18]. If \mathbf{r} is the vector connecting two spheres, then the force acting between these spheres is given by

$$\mathbf{f} = k(r-l) \frac{(r_+ - l)(l - r_-)}{(r_+ - r)(r - r_-)} \frac{\mathbf{r}}{r}, \quad \text{for } r_- < r < r_+, \quad (2)$$

where $r = |\mathbf{r}|$ is the distance between the spheres, l the equilibrium length of the spring, k the spring constant describing the Hookean behavior of the spring for small extensions about the equilibrium length and $s < 1$ is a nonlinearity parameter of the spring. At the extensions

$$r_{\pm} = (1 \pm s)l, \quad (3)$$

the force diverges so that the bond length between two spheres is restricted to the indicated, finite range.

In contrast to [17], here we choose *identical* force parameters k and s for the bonds; only the equilibrium bond lengths l may differ. Hence, possible chirality of the equilibrium configuration of an object is solely determined by its geometry: according to the standard definition, the configuration of an object is *achiral* if a movement of the object, i.e. a combination of translations and rotations in 3D space, exists such that it matches its mirror image; in any other case the configuration is *chiral*.

When the object is suspended in a flowing fluid, advective forces act on the individual spheres, which in addition mutually influence their motions by hydrodynamic interactions. The total action of the fluid on the sphere will be described by a mobility tensor $\mathbf{H}_{n,m}$ relating the forces acting on the m th particle to the velocity of the n th particle. The

deterministic, overdamped motion of the object in a fluid flow with the velocity field $\mathbf{v}(\mathbf{r})$ is then given by

$$\dot{\mathbf{r}}_n = \mathbf{v}(\mathbf{r}_n) + \sum_{m=1}^4 \mathbf{H}_{n,m} \cdot \mathbf{f}_m, \quad (4)$$

where \mathbf{f}_m is the total force acting on the m th sphere, i.e. the sum of the FENE-Fraenkel forces (2) exerted by the other three spheres, and the dot denotes differentiation with respect to time. For sufficiently small spheres, inertial terms can be neglected [19]. We shall describe the mobility by the Rotne–Prager tensor which includes the hydrodynamical interactions up to second order in the ratio $a/r_{n,m}$ of the sphere radius a and the distance $r_{n,m}$ between the n th and the m th sphere. It is given by [20]

$$\mathbf{H}_{n,m} = \frac{1}{6\pi\eta a} \left[\delta_{n,m} \mathbb{1} + (1 - \delta_{n,m}) \frac{3a}{4r_{n,m}} \mathcal{H}_{n,m} \right], \quad (5)$$

with

$$\mathcal{H}_{n,m} = \begin{cases} \left(1 + \frac{2a^2}{3r_{n,m}^2}\right) \mathbb{1} + \left(1 - \frac{2a^2}{r_{n,m}^2}\right) \frac{\mathbf{r}_{n,m}\mathbf{r}_{n,m}}{r_{n,m}^2}, & \text{for } r_{n,m} \geq 2a, \\ \left(1 - \frac{9r_{n,m}}{32a}\right) \mathbb{1} + \frac{3\mathbf{r}_{n,m}\mathbf{r}_{n,m}}{32ar_{n,m}}, & \text{for } r_{n,m} < 2a, \end{cases} \quad (6)$$

where $\mathbb{1}$ denotes the unit tensor in 3D space, η the viscosity of the fluid and $\mathbf{r}_{n,m} = \mathbf{r}_m - \mathbf{r}_n$ the vector pointing from the position of the n th to that of the m th sphere.

In passing, we mention that thermal noise leads to additional random contributions in the equations of motion, yielding [21]

$$\dot{\mathbf{r}}_n = \mathbf{v}(\mathbf{r}_n) + \sum_{m=1}^4 \mathbf{H}_{n,m} \mathbf{f}_m + \sqrt{2k_B T} \sum \boldsymbol{\sigma}_{n,m} \cdot \boldsymbol{\xi}_m(t), \quad (7)$$

where $\boldsymbol{\xi}_n(t)$ are mutually independent 3D Gaussian, white noise vectors satisfying

$$\langle \boldsymbol{\xi}_n(t) \boldsymbol{\xi}_m(s) \rangle = \delta_{n,m} \mathbb{1} \delta(t - s). \quad (8)$$

The fluctuation–dissipation theorem requires that the coupling to the noise, $\boldsymbol{\sigma}_{i,j}$, be related to the Rotne–Prager tensor according to

$$\mathbf{H}_{n,m} = \sum_{k=1}^4 \boldsymbol{\sigma}_{n,k} \cdot \boldsymbol{\sigma}_{m,k}. \quad (9)$$

In this work however, we neglect all influences stemming from thermal noise. This requires that the radius of the spheres, constituting objects with parameters as specified below, be at least $1 \mu\text{m}$ in order that thermal fluctuations can be neglected as compared to the hydrodynamic interactions in water at room temperature flowing with a uniform shear rate $\kappa = 1 \text{ s}^{-1}$. In the following, we restrict ourselves to a discussion of the deterministic equations of motion in (4). We shall consider a uniform shear flow given by

$$v_x = v_y = 0, \quad v_z = \kappa y, \quad (10)$$

where κ denotes the shear rate; see figure 1(b). Even in this seemingly simple case the deterministic equations of motion can only be solved by a numerical means. For that purpose,

we employed an LSODA code of variable order and step length [22, 23] as available from the open source SciPy package [24].

In the numerical treatment, we used dimensionless variables where lengths are measured in units of the sphere radius a and times in units of the inverse shear rate κ^{-1} . Apart from six parameters that fix the equilibrium geometry of an object consisting of four spheres in general, or three in the present case of a spiral object as defined by equation (1), two further parameters are needed for the characterization of the forces. As such we will choose the nonlinearity parameter s and the dimensionless spring constant $k_f = k/(6\pi\eta a\kappa)$. With this choice the deterministic equations of motion read

$$\dot{\mathbf{x}}_n = \mathcal{S}\mathbf{x}_n + k_f \sum_{m=1}^4 \mathcal{H}_{n,m} \cdot \mathbf{F}_m, \quad (11)$$

where \mathcal{S} is the shear tensor, which has vanishing matrix elements apart from the z - y element, being unity, and \mathbf{F}_m denotes the dimensionless force exerted on the m th particle by the adjacent particles, reading

$$\mathbf{F}_m = \sum_{n \neq m} \frac{x_{n,m} - \ell_{n,m}}{1 - (1 - x_{n,m}/\ell_{n,m})^2/s^2} \frac{\mathbf{x}_{n,m}}{x_{n,m}} \quad \text{for } (1-s)\ell_{n,m} < x_{n,m} < (1+s)\ell_{n,m}. \quad (12)$$

Here $\mathbf{x}_n = \mathbf{r}_n/a$, $\mathbf{x}_{n,m} = \mathbf{x}_n - \mathbf{x}_m$, $x_{n,m} = |\mathbf{x}_{n,m}|$ and $\ell_{n,m} = |\mathbf{R}_n - \mathbf{R}_m|/a$ denote the dimensionless positions, distance vectors, the actual distances and the equilibrium distances between spheres n and m , respectively.

Possible initial conditions for the integration of the equation of motion (11) are given by any set of sphere positions that obey the restrictions imposed by the FENE-Fraenkel forces (12). Here we confine ourselves to equilibrium configurations of the free objects. For further details of how the orientations are chosen, see section 3.

2.2. Characteristics of the mechanical state of an object

In the framework of the overdamped dynamics of equation (11) the mechanical state of the object is uniquely described by the positions $\mathbf{x}_n(t)$ of the four spheres. A reduced description is provided by the center of mass of the object consisting of four spheres of equal mass, consequently reading

$$\mathbf{X} = \frac{1}{4} \sum_n \mathbf{x}_n. \quad (13)$$

The spatial orientation of the object can conveniently be characterized by the three principal axes of the symmetric tensor of second moments of the sphere positions, \mathbf{M} , defined by its elements

$$M_{i,j} = \frac{1}{4} \sum_n (x_i^n - X_i)(x_j^n - X_j), \quad (14)$$

where x_i^n denotes the i th Cartesian position component of the n th sphere. The orientations of the principal axes are determined by the normalized eigenvectors \mathbf{u}_i and their magnitudes by the corresponding eigenvalues λ_i of the tensor of second moments. Hence, they result from the

eigenvalue problem

$$\mathbf{M}\mathbf{u}_i = \lambda_i \mathbf{u}_i, \quad (15)$$

where $\mathbf{M} = (M_{i,j})$.

The velocity vector $\boldsymbol{\omega}$ of the instantaneous rotation of the object in the frame co-moving with the object's center of mass is determined by the orientation and velocity of any body-fixed tripod. Here we use the principal axes of the second moments to obtain

$$\boldsymbol{\omega} = -\frac{1}{2} \sum_i \dot{\mathbf{u}}_i \times \mathbf{u}_i, \quad (16)$$

where the dot denotes a derivative with respect to time and $\mathbf{u} \times \mathbf{v}$ the vector product of the vectors \mathbf{u} and \mathbf{v} . By means of the eigenvalue equation (15) one may express $\dot{\mathbf{u}}_i$ in terms of the time derivative of \mathbf{M} , to yield

$$\boldsymbol{\omega} = \frac{1}{2} \sum_{i \neq j} \frac{\mathbf{u}_j \cdot \dot{\mathbf{M}} \mathbf{u}_i}{\lambda_j - \lambda_i} \mathbf{u}_j \times \mathbf{u}_i, \quad (17)$$

where $\mathbf{u} \cdot \mathbf{v}$ denotes the scalar product of the vectors \mathbf{u} and \mathbf{v} .

As a measure of the deformation of an object, we consider the ratio of volumes taken in the distorted state and the equilibrium shape. As object volume one may assign the square root of the product of the magnitudes of the principal axes, i.e.

$$V = (\lambda_1 \lambda_2 \lambda_3)^{1/2}. \quad (18)$$

Whether an object is chiral cannot be decided on the basis of its second moments of positions. For this purpose, we use the isotropic chirality index G_0 , which is invariant under translations and rotations of the object [25], in its dilation invariant form. For an object consisting of four spheres of equal mass and size it becomes

$$G_0 = \frac{1}{3} \sum_{i,j,k,l} \frac{\mathbf{x}_{i,j} \cdot (\mathbf{x}_{k,l} \times \mathbf{x}_{i,l}) (\mathbf{x}_{i,j} \cdot \mathbf{x}_{j,k}) (\mathbf{x}_{j,k} \cdot \mathbf{x}_{k,l})}{(x_{i,j} x_{j,k} x_{k,l})^2 x_{i,l}}. \quad (19)$$

The sum is extended over all sets i, j, k, l taken from the permutations of $\{1, 2, 3, 4\}$. This index has the general property that it assumes the same absolute value but opposite signs for enantiomers, i.e. pairs of configurations that are mirror images of each other. Hence, achiral configurations have a vanishing chirality index.

For a spiral object, the chirality index is a function of the relative rise ρ/h and the screw angle φ . It is an antisymmetric function about the line $\varphi = \pi$, see figure 2(a), and possesses a singularity at $\varphi = 2\pi/3$ and $h/\rho = 0$. Along the lines $h/\rho \approx -(\varphi - 2\pi/3)$ for $\varphi < 2\pi/3$ and $h/\rho \approx 0.95(\varphi - 2\pi/3)$ for $\varphi > 2\pi/3$ the chirality index forms a ridge and a valley, respectively. Approaching the singularity along the ridge, the chirality index converges to the approximate value 0.289, while it approaches the opposite value -0.289 along the bottom of the valley.

Since all configurations with $h/\rho = 0$ are planar and hence achiral, the chirality index exactly vanishes on the line $h/\rho = 0$. In the remaining part of the φ - h/ρ -plane, the chirality index has three extrema on each side of the symmetry line $\varphi = \pi$. Local extrema are located at $\varphi \approx 0.8908\pi$, $h/\rho \approx 0.2073$ and $\varphi \approx 0.9291\pi$, $h/\rho \approx 0.584$. The absolute maximum is at $\varphi \approx 0.656\pi$, $h/\rho \approx 2.516$; see figure 2(a). The chirality index vanishes on the solid and dashed curves in figure 2(b). These curves result from constraints on the bond lengths (see the appendix). Along the dashed curve emerging from $\varphi = \pi/2$, $h/\rho = 0$ and ending in $\varphi = \pi$,

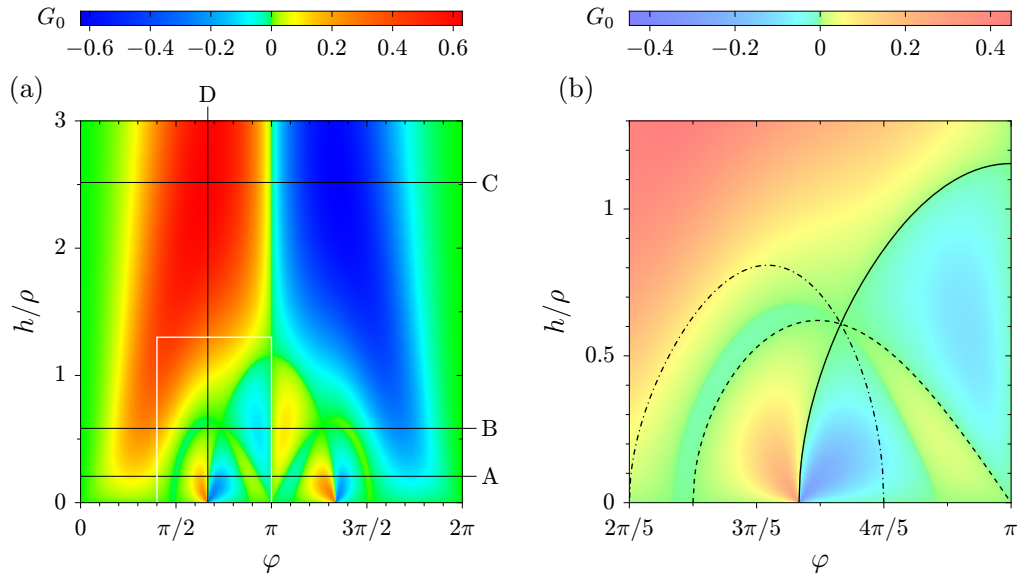


Figure 2. The chirality index G_0 defined in equation (19) is displayed for spiral objects as a function of the screw angle φ and the relative rise h/ρ ; see equation (1). In panel (a) the symmetry $G_0 \rightarrow -G_0$ upon a reflection on the line $\varphi = \pi$ is clearly visible. The four black lines labeled by A–D indicate four cuts through the parameter plane; see the text in section 3 as well as figure 5. The lines A and B are defined by local maxima of the chirality index. On C and D the absolute maximum of G_0 is located. Panel (b) represents a blow-up of the region marked in panel (a) by the white lines. Note that for the purpose of better visibility, different color scales are used in the two panels. The black lines in panel (b) indicate those curves on which two of the three edge lengths $l(k)$, $k = 1, 2, 3$ between spheres with positions \mathbf{R}_n and \mathbf{R}_{n+k} are equal; see the [appendix](#). The solid line represents achiral configurations with $l(1) = l(2)$ which have five equally long edges. It starts at the singularity of G_0 at $\varphi = 2\pi/3$ and $h/\rho = 0$ and ends at $\varphi = 4\pi/3$ and $h/\rho = 0$. Along the dashed line, $l(1) = l(3)$ holds. These configurations have two and four equally long edges and are also achiral. On the dashed-dotted line, where $l(2) = l(3)$, the configurations possess two triples of equally long edges, and the chirality index is nonzero everywhere except at the points with $h/\rho = 0$ and at the crossing point of the three lines which correspond to a regular tetrahedron. Note that there is still a third curve recognizable by the green color on which the chirality index vanishes in spite of the chirality of the corresponding configurations.

$h/\rho = 0$, the configurations possess a group of four and another one of two equally long edges; see figure 3(b). Since the corresponding configurations exhibit a symmetry plane, they are achiral. The faces of these tetrahedra are made of identical isosceles triangles. Also the configurations on the curve starting at $\varphi = 2\pi/3$, $h/\rho = 0$ and reaching $\varphi = \pi$, $h/\rho = 2/\sqrt{3}$ are achiral; the faces of these configurations consist of two identical equilateral and two identical isosceles triangles; consequently, five of the six edges have the same length; see figure 3(c). The analytic forms of the achiral curves are derived in the [appendix](#). Examples of different types of

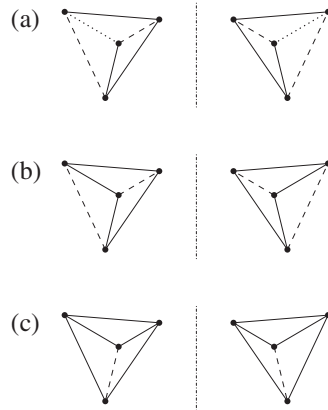


Figure 3. Panel (a) illustrates a generic spiral object with three and two edges of equal lengths and a sixth edge of a different length. The edges of equal lengths are drawn correspondingly. Panel (b) presents a configuration on the dashed curve displayed in figure 2(b) with two and four equally long edges, while the configuration in panel (c) has five equally long edges representing a configuration on the solid curve depicted in figure 2(b). The right part of the figure represents the corresponding mirror images. The cases (b) and (c) are achiral.

configurations are displayed in figure 3. There exists a third node line of G_0 which, however, does not correspond to achiral configurations. We could not find an analytic expression for this line which emerges from $\varphi \approx 0.46\pi$, $h/\rho = 0$ and ends in $\varphi \approx 0.88\pi$, $h/\rho = 0$. The three node lines of the chirality index meet in a single point which corresponds to a regular tetrahedron. For the fact that a vanishing value of the chirality index does not necessarily correspond to an achiral configuration, see [26].

3. Results

For our investigations, we selected configurations of spiral objects corresponding to four cuts in the parameter plane displayed in figure 2(a). Three of these cuts (A, B and C) are taken at constant relative rise $h/\rho = 0.2073$, 0.584 and 2.5162 , respectively, each for $\varphi \in (0, \pi)$. For the two smaller values of h/ρ we chose a relatively large radius $\rho = 7$ in order to avoid any collision of the spheres within an object, and the smaller radius $\rho = 2$ for the large relative rise. The vertical cut D is determined by the screw angle $\varphi = 2\pi/3$, radius $\rho = 3$ and relative rise $h/\rho \in (0, 5)$.

As initial configurations we took the equilibrium configurations according to equation (1), rigidly translated such that the center of mass falls at the origin. Finally, rigid rotations of the object about its center of mass were performed. Between 500 and 5000 rotations were sampled from the uniform distribution of the 3D rotation group², i.e. from the Haar measure of $SO(3)$.

² In order to draw elements out of the Haar measure of $SO(3)$, we first generate a random vector with three independent Gaussian components about which a rotation with an angle α is performed. To guarantee a uniform coverage of the rotation group, the rotation angle $\alpha \in [0, \pi]$ must be drawn from the probability density $(1/\pi)\sin^2(\alpha/2)$ [27].

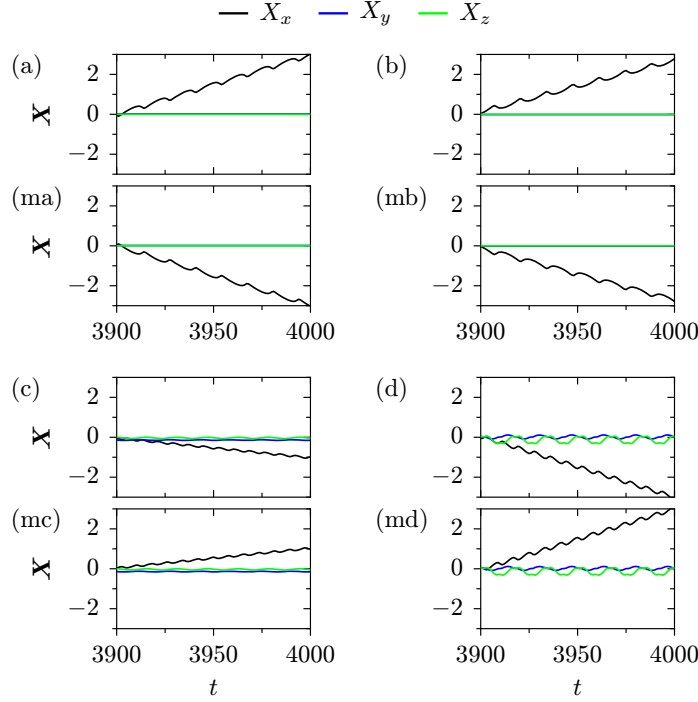


Figure 4. The center of mass motion of a spiral object with an equilibrium configuration on cut A specified by $h/\rho = 0.2073$, $\rho = 7$ and $\varphi = 0.87\pi$ asymptotically reaches one of the four different states depicted in panels (a)–(d) depending on the initial orientation of the object. If this orientation is randomly drawn from a uniform distribution, then one finds the cases (a) with a probability of 0.19, (b) with 0.22, (c) with 0.50 and (d) with 0.09. The x -component of the center of mass is displayed in black. It is shifted by its actual value taken at time $t = 3900$; the y -component, which is either constant or periodically oscillating, is depicted by the blue line; from the z -component (green) an average uniform motion is subtracted. The configurations mirrored in the y – z -plane starting from the corresponding mirror images of the initial orientations of (a)–(d) result in the motion patterns displayed in panels (ma)–(md), which obviously coincide with the mirror images of panels (a)–(d). The average velocities $\langle v_x \rangle$ in the x -direction, see equation (20), in the cases (a) and (ma) are ± 0.02974 ; correspondingly one finds that $\langle v_x \rangle = \pm 0.02594$ in (b) and (mb), $\langle v_x \rangle = \mp 0.00994$ in (c) and (mc) and $\langle v_x \rangle = \mp 0.03044$ in (d) and (md). In all cases the mirrored patterns occur with the probabilities of the corresponding original ones as specified above.

We typically let run each trajectory for 4000 time units [κ^{-1}]. In the majority of the cases the trajectories have relaxed toward an asymptotic regime long before the end of the time span of 4000. In this state, the center of mass acquires a finite velocity in the z -direction, depending on the precise initial position of the object, and the y -component of the velocity may perform small oscillations but vanishes on average. The lateral motion in the direction of the vorticity, coinciding with the x -direction in the present case, is characterized by an average velocity superimposed by bounded modulations, which were always periodic. Figure 4 displays the

components of the center of mass for the same object and its mirror image in four different asymptotic motional states.

3.1. Center of mass motion

The fact that the x -component of the center of mass moves at a finite average velocity is apparently related to the chirality of the considered object: for any achiral object in the considered shear flow the opposite x -directions are equivalent. This symmetry is broken by the presence of a chiral object and, according to the Curie principle [28], the object will perform a directed motion in either of the two directions. This argument is further corroborated if one launches the chiral partner of a considered object into the shear flow with initial sphere positions obtained from the original ones by mirroring on the y - z -plane. Then one indeed finds the object moving in the opposite x -direction as illustrated by the panel pairs ((a), (ma)) and ((b), (mb)), etc in figure 4 displaying the corresponding pairs of mirror images.

Inserting an object into the shear flow with randomly chosen orientations as described above, one typically finds between one and four different motional states of the center of mass, which are asymptotically reached at large times. We determined the corresponding average velocities $\langle v_x \rangle$ by a least-square fit of the x -components of the center of mass to a uniform motion, yielding

$$\langle v_x \rangle = \frac{12}{N(N+1)(N+2)\tau} \sum_{n=0}^N \left(n - \frac{N}{2} \right) X_x(t_0 + n\tau). \quad (20)$$

In most cases, we used $t_0 = 3000$, $N = 1000$ and $\tau = 1$. Since the different motional states typically are distinguished by their average velocities, these velocities may be used to roughly classify the asymptotic states as exemplified in figure 5. A precise classification would require additional knowledge of the object's orientation and six bond lengths and, hence, would be difficult to visualize.

In addition to the average center of mass velocity, the behavior of the chirality index G_0 of the initial configuration is depicted by the red line in figure 5 along the respective cuts. This index correlates with the average velocities at best in a qualitative way. Of particular interest here is the behavior of the average velocity in the vicinities of the zeros of the chirality index as a function of the screw angle φ indicated by the blue lines.

As mentioned at the end of section 2, one has to distinguish between chiral and achiral zeros of the chirality index G_0 . Indeed, close to chiral zeros, none of the three existing velocity branches crosses the zero line. But also near the achiral zeroes, branches with finite velocities may exist. They may coexist with a branch with vanishing average velocity, which, however, may also be missing. The $x \leftrightarrow -x$ -inversion symmetry however is restored on average since there are always pairs of branches with opposite velocities which are populated with equal probability. As we shall discuss in more detail below, the branches with finite average velocities at achiral zeros of the chirality index represent states of dynamically broken symmetry.

3.2. Rotational motion

In the asymptotic state, when the center of mass undergoes a periodically modulated uniform motion, the instantaneous rotation axis predominantly points in the x -direction, possibly superimposed by small, oscillatory deviations orthogonal to this direction. Figure 6 depicts

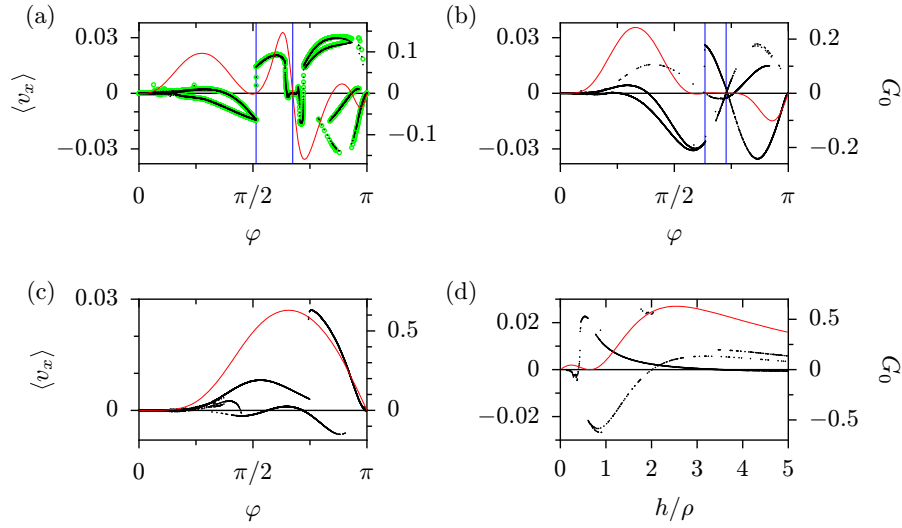


Figure 5. Asymptotic average velocities $\langle v_x \rangle$ were estimated for objects with equilibrium configurations along the four cuts A–D in the φ – h/ρ parameter plane displayed in figure 2(a). The initial conditions were randomly oriented according to the uniform measure on the 3D rotation group. Panels (a)–(c) correspond to the horizontal cuts A, B, C along $h/\rho = 0.2073$ with $\rho = 7$ and $h/\rho = 0.584$ with $\rho = 7$ and $h/\rho = 2.5162$ with $\rho = 3$, respectively. Panel (d) represents the vertical cut D for $\varphi = 2\pi/3$, $\rho = 5$ and $h/\rho \in (0, 5)$. For comparison, the chirality index G_0 defined in equation (19) is depicted by a red line with the corresponding scale at the right-hand side ordinate. The vertical blue lines in panels (a) and (b) mark the respective values of the screw angles at which the equilibrium configurations are achiral. In all panels, black dots represent the result of the solution to the equations of motion (11) with the full Rotne–Prager tensor (6). The average velocities group into up to four well-defined branches at most parameter values. In panel (a), additionally the numerical results obtained from equation (11) with the Oseen tensor (25) are displayed as small green circles. The overall agreement between the two approaches is very good; see also section 4.

the components of the instantaneous rotation axis for different asymptotic motional states of the same object. This orientation of the instantaneous rotation axis appears as a rather natural consequence of the considered flow geometry with uniform vorticity pointing in the x -direction. Conspicuous tumbling behavior of the instantaneous rotation axis was found in the case of dynamically broken symmetry; see figure 12(a). The rotation speed undergoes pronounced oscillations in the majority of cases. In the asymptotic states in which the instantaneous rotation axis points in the x -direction the object is typically found to be oriented such that one of its principal axes is aligned with the direction of rotation. The transient behavior toward the specific asymptotic states of the angle enclosed by the principal axes and the instantaneous rotation axis is illustrated in figure 7.

Due to the lack of any symmetry plane in a chiral object, there are two distinct ways to orient a principal axis along the instantaneous axis of rotation. However, we found different velocity branches corresponding to opposite orientations only for alignments of the rotation

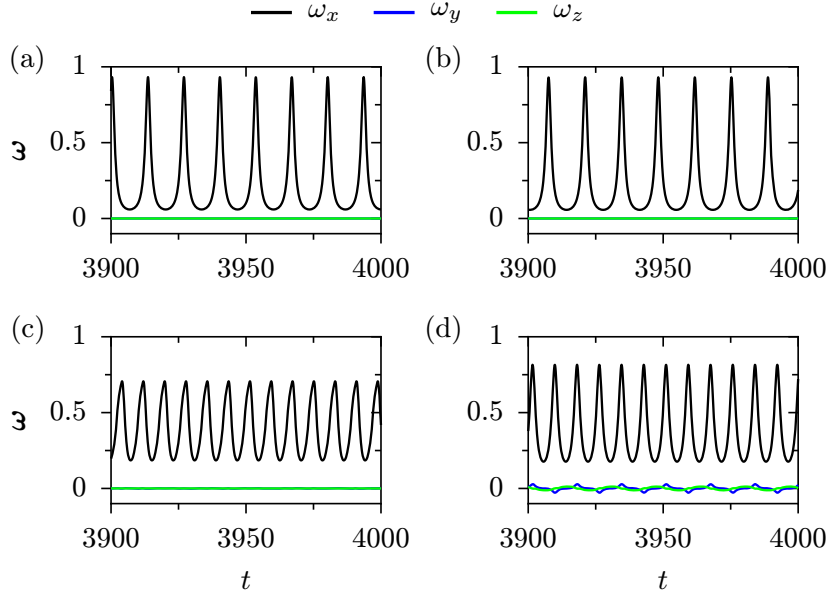


Figure 6. The components of the instantaneous axis of rotation, ω , for the configuration with $\varphi = 0.87\pi$, $h/\rho = 0.2073$ and $\rho = 7$ corresponding to the maximum of G_0 on cut A. The component ω_x pointing in the vorticity direction of the shear flow is marked in black and the y- and z-components in blue and green, respectively. Panels are labeled as in figure 4. In all cases the rotation about the vorticity direction is dominant. Only in panel (d) is a slight tumbling of the axis noticeable.

axis with the middle principal axis and only if the skewness S_ω of the object along the axis of rotation vanishes within numerical precision. As a measure of the skewness of an object relative to the vector of angular velocity ω , we take the third root of the third moment of the sphere positions \mathbf{x}_n relative to the center of mass projected onto the direction of the rotation axis, $\mathbf{e}_\omega = \omega/|\omega|$, hence reading

$$S_\omega = \left(\sum_n \left((\mathbf{x}_n - \mathbf{X}) \cdot \mathbf{e}_\omega \right)^3 \right)^{1/3}. \quad (21)$$

The maximum number of branches we detected was four. For $\eta/\rho = 0.2073$, $\rho = 7$ and screw angles approximately ranging between $\varphi = 0.8\pi$ and $\varphi = 0.9\pi$, one observes single alignments to the small and the large axes and both orientations relative to the middle axis. Figure 8 represents the time evolution of the skewness for an object with initial orientations belonging to different domains of attraction.

3.3. Internal motion and dynamical symmetry breaking

Also in the reference frame that moves with the center of mass and rotates with the instantaneous angular velocity, the objects generally are not at rest but undergo internal motions characterized by changing bond lengths and bond angles. These distortions then lead to modulations of the magnitudes of the principal axes as illustrated in figure 9. The resulting periodic relative volume changes of the object are presented in figure 10.

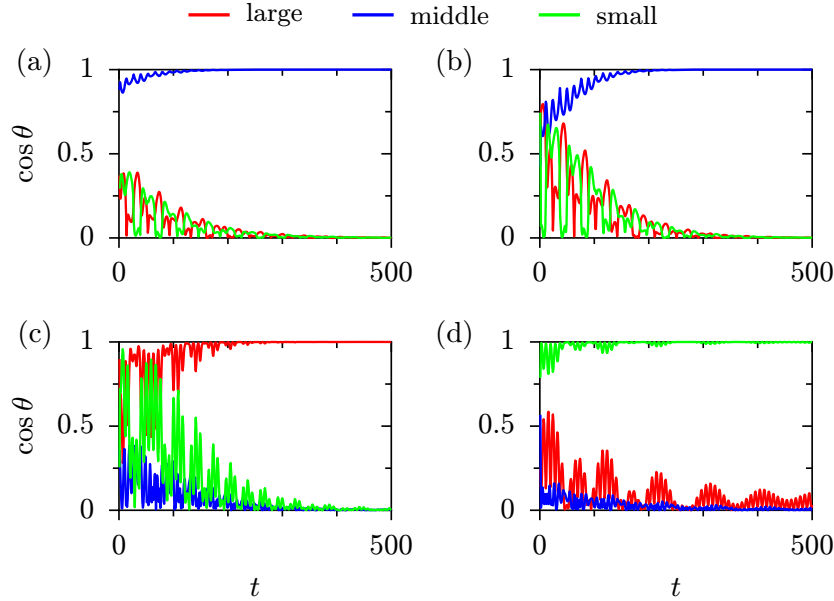


Figure 7. The time evolution of the cosines of the angles between the instantaneous vector of rotation and the eigenvectors of the second moments of positions, $\cos \theta_i = \boldsymbol{\omega} \cdot \mathbf{u}_i / |\boldsymbol{\omega}|$, for the configuration with $\varphi = 0.87\pi$, $h/\rho = 0.2073$ and $\rho = 7$ is depicted for different initial orientations. The asymptotic motion of the center of mass as well as the motion of the axes of instantaneous rotations are displayed in figures 4 and 6, respectively, with the panels labeled consistently. The cosine of the eigenvector corresponding to the largest eigenvalue is displayed in red, to the middle one in blue and to the smallest one in green. In panels (a) and (b), the middle principal axis asymptotically aligns with the rotation axis, while the initial orientations in panels (c) and (d) lead to alignments with the largest and the shortest axis, respectively.

3.3.1. Dynamical symmetry breaking. A deformation of objects with achiral equilibrium configurations, caused by shear forces, in general will break their mirror symmetry and hence render the objects chiral. This mechanism is at the heart of the effect of *dynamical symmetry breaking* that can be observed at achiral zeros of the chirality index G_0 .

For spiral objects the 3D achiral configurations are found on two curves in the φ – h/ρ -parameter plane, reading

$$(h/\rho)_1 = \left[\frac{2}{3} (\cos(2\varphi) - \cos(\varphi)) \right]^{1/2}, \quad 2\pi/3 < \varphi < 4\pi/3, \quad (22)$$

$$(h/\rho)_2 = \frac{1}{2} [(\cos(3\varphi) - \cos(\varphi))]^{1/2}, \quad \pi/2 < \varphi < 3\pi/2. \quad (23)$$

For a derivation see the [appendix](#). The branch $(h/\rho)_1$ corresponds to the solid line and $(h/\rho)_2$ to the dashed line in figure 2(b). Figure 11(a) displays the asymptotic average velocities in the x -direction and the corresponding average values of the chirality index for the achiral configuration at $\varphi = 0.7271607\pi$ and $\rho = 7$ on the curve $(h/\rho)_1$. As for all achiral configurations on this curve, it possesses five equally long edges. In the present case, the sixth edge is shorter than the others. This object is initially oriented in such a way that the symmetry plane containing both the short edge and the z -axis encloses an angle α with the y -axis; see figure 11(b). Depending on this angle α , two different pairs of asymptotic states with

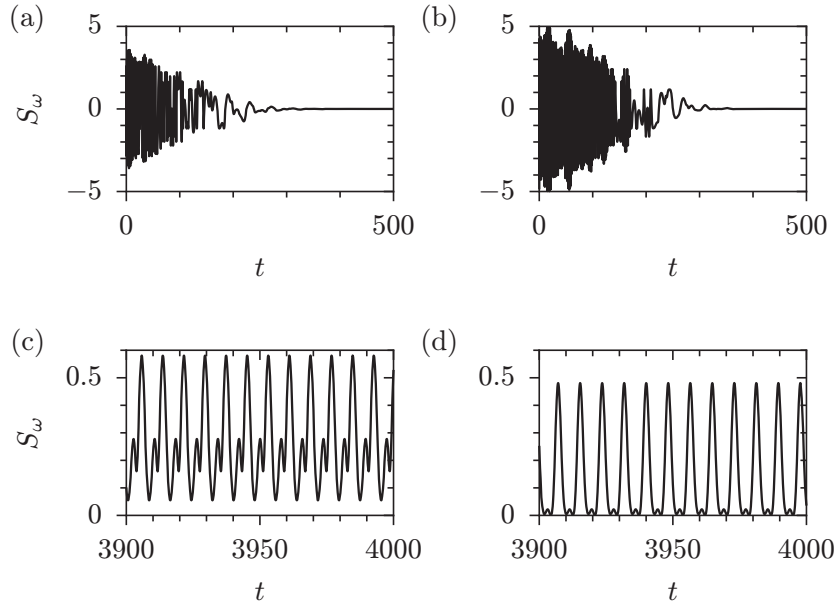


Figure 8. For those initial orientations of the configuration with $\varphi = 0.87\pi$, $h/\rho = 0.2073$ and $\rho = 7$ which finally approach two different states both rotating about the middle axis, see figures 7(a) and (b), the third moments of the positions projected onto the instantaneous axis of rotation, S_ω , defined in equation (21), relax to zero. For other initial orientations the skewness S_ω asymptotically undergoes rotations; see panels (c) and (d).

non-vanishing velocities and chirality indices of opposite signs are approached with time. The average chirality index was obtained as an algebraic mean over a time window of length 1000 in the asymptotic regime. Because a rotation about the z -axis by $\alpha = \pi$ leaves any of these initial configurations invariant, the resulting pattern of average velocities and chirality indices is periodic with period π . The rotational motion and the orientation of the principal axes are presented in figure 12 for two of the chiral attractors of an achiral object.

The average asymptotic velocities were determined on a part of the achiral curve $(h/\rho)_1$ given by equation (22) for $\rho = 5$. Similarly as on the other cuts, equilibrium configurations were obtained from equation (1) at 2001 equally spaced angular values for $\varphi \in [0.67\pi, \pi]$; subsequently, their centers of mass were translated into the origin and randomly rotated about the center of mass. With these initial conditions the equations of motion were integrated up to $t = 8000$. The average velocity $\langle v_x \rangle$ was calculated according to equation (20) for $t_0 = 7000$, $N = 1000$ and $\tau = 1$. Figure 13 presents the resulting averaged velocities in the x -direction. The emerging pattern is essentially symmetric about $\langle v_x \rangle = 0$ and consists of different branches and a region with a cloud of apparently random points. The deviations from symmetry are insignificant within statistical uncertainty. Whereas, on the branches, the center of mass approaches an average motion with constant velocity $\langle v_x \rangle$, superimposed by short oscillations, in the cloud region it asymptotically oscillates with a period which is larger than the width of the averaging window; see figure 14. Hence, the resulting averages over a window that is shorter than a period are randomly distributed within an upper and a lower bound. The true averages extended over a full period are zero within numerical precision.

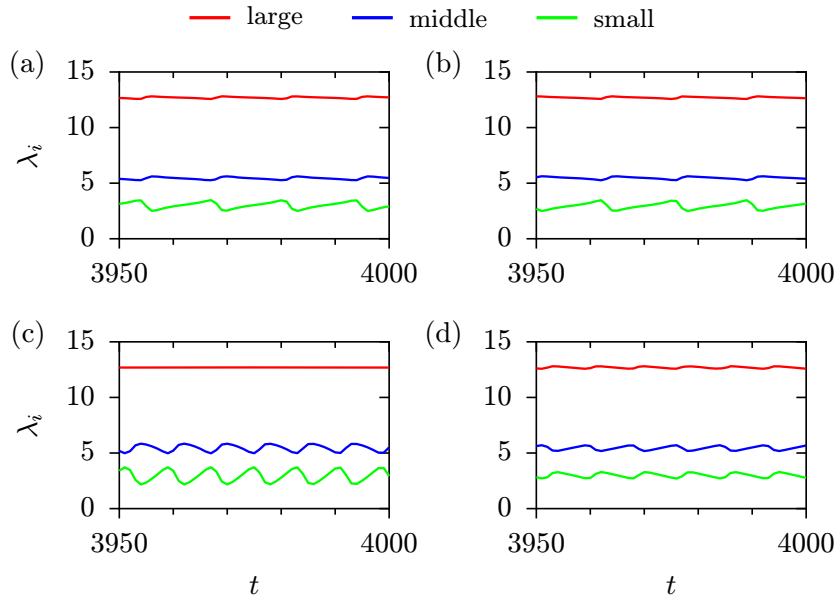


Figure 9. The magnitude of the principal axes of the second moments of position for the configuration with $\varphi = 0.87\pi$, $h/\rho = 0.2073$ and $\rho = 7$. In the four different asymptotic states, which are labeled in the same way as in the previous figures, the magnitudes of the principal axes undergo periodic modifications. In the two cases with positive asymptotic velocities, (a) and (b), these modifications are almost identical. Noticeable differences occur between the states characterized by rotations about the large and the short principal axes, displayed in panels (c) and (d), respectively.

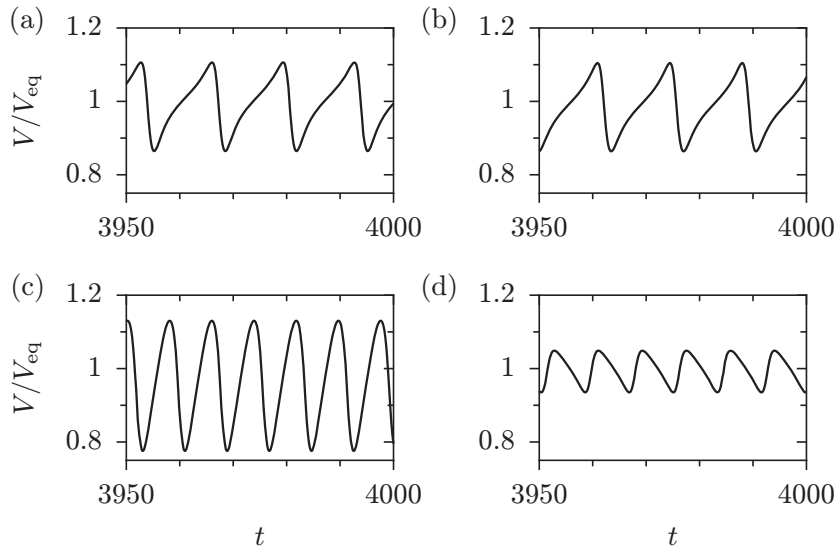


Figure 10. The ratio of the actual to the equilibrium volume for different initial orientations of the configuration with $\varphi = 0.87\pi$, $h/\rho = 0.2073$ and $\rho = 7$ in the same order as in figures 6–9. For the two asymptotic states (a) and (b) moving in the positive x -direction, the volume variations are essentially identical but different from both states (c) and (d).

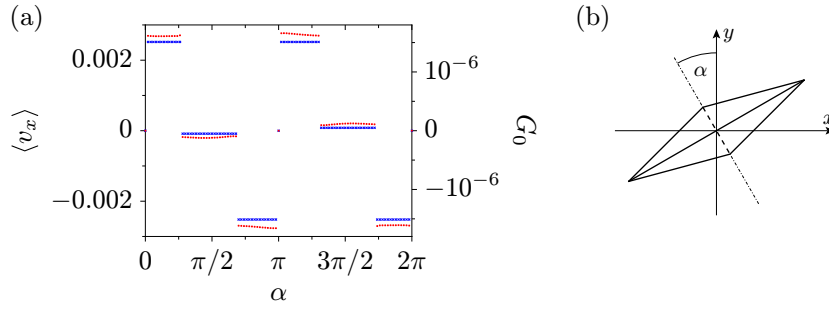


Figure 11. In panel (a), different chiral-symmetry breaking attractors for the achiral equilibrium configuration at $\varphi = 0.727\,1607\pi$, $h/\rho = 0.584$ and $\rho = 7$ are characterized by their average velocities $\langle v_x \rangle$ (blue) and average chirality indices $\langle G_0 \rangle$ (red). The attractors are approached from different orientations of the object. The angle α specifying the initial orientation is enclosed by the y -axis and the object's symmetry plane containing the short edge of the object as exemplified in panel (b), which presents a view with the z -axis perpendicular to the plane of projection. For $\alpha = 0$ the y - z -plane coincides with the symmetry plane of the object.

As in the case of chiral equilibrium configurations, in the case of achiral equilibrium configurations the number of branches varies from one up to four in the present investigation. In the limiting cases of $\varphi = 2/3\pi$ and $\varphi = \pi$ the configurations on the achiral curve are planar and only a single branch with $\langle v_x \rangle = 0$ exists. Additional branches appear for intermediate values of φ always in pairs with positive and negative velocities and opposite chirality indices, while the zero-velocity and zero-chirality-index branches may become unstable. Branches with opposite velocities and chirality indices always occur with equal weight such that the mirror symmetry of the initial achiral configuration is restored. For $\varphi = \arccos(-2/3) \approx 0.732\pi$, corresponding to a regular tetrahedron, four velocity branches cross each other at $\langle v_x \rangle = 0$; see figure 13.

The present phenomenon of *dynamical symmetry breaking* is different from that reported in [17], where objects with initially achiral geometric configurations but with different bond strengths were considered. Hence those objects were chiral from the outset with respect to their mechanical properties. We emphasize here that the effect of dynamical symmetry breaking occurs for achiral objects with respect to both geometry and bond strengths.

4. Role of hydrodynamic interactions

In order to clarify the role of hydrodynamic interactions for the transport of chiral objects in a shear flow, we compared the motion of a spiral object with screw angle $\varphi = \pi/2$, relative rise $h/\rho = 0.584$ and radius $\rho = 7$ in the presence of three different vector fields describing the action of the fluid on the object at different levels of accuracy. In the crudest approximation, the forces contribute to the velocity in terms of the Stokes law, for which the mobility tensor simplifies to

$$\mathbf{H}_{i,j}^{\text{Stokes}} = \frac{1}{6\pi\eta a} \mathbb{1}_{\delta_{i,j}}. \quad (24)$$

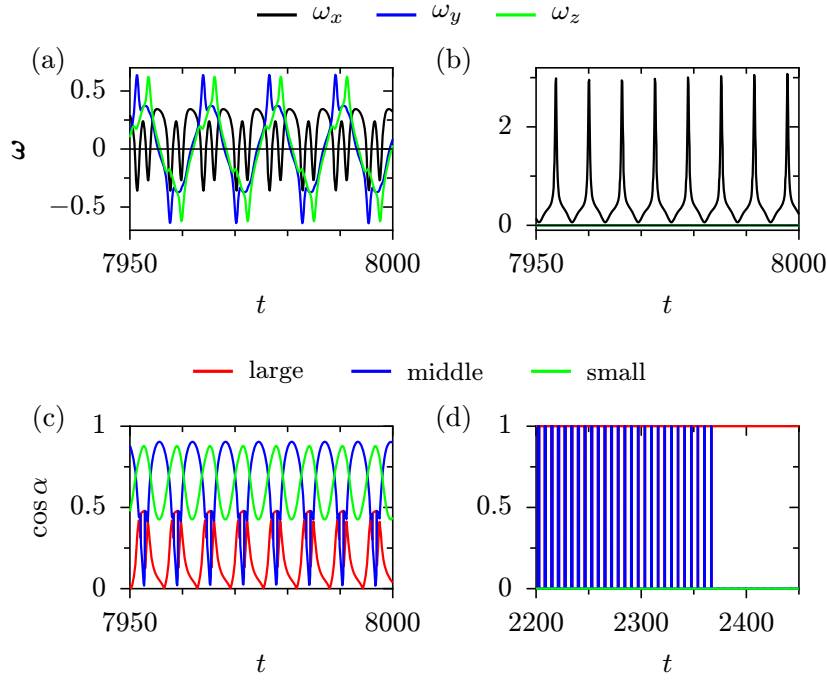


Figure 12. Different modes of the rotational motion of an object with $\varphi = 0.727\,1607\pi$, $h/\rho = 0.584$ and $\rho = 7$ corresponding to an achiral equilibrium configuration on the $(h/\rho)_1$ -curve. In the upper row the components ω_x (black), ω_y (blue) and ω_z (green) of the instantaneous rotation axis are displayed; the lower row presents the cosines of angles between the large (red), middle (blue) and small (green) principal axes and the x -axis. The left column corresponds to the asymptotic state with larger positive velocity in the x -direction $\langle v_x \rangle = 0.0025$ and the right column to the asymptotic state with smaller positive velocity in the x -direction, $\langle v_x \rangle = 0.000\,083$. In the case of the large positive velocity, the object performs a tumbling but periodic motion as can be seen both from the oscillatory behavior of the instantaneous rotation axis (a) and from the alignment of the instantaneous axis with the x -axis (c). In the asymptotic state of slow motion, the instantaneous rotation axis exactly points in the x -direction (b). Asymptotically (for times $t > 2360$), the large principal axis strictly lies in the x -direction (d). In a transient period at earlier times the object orientation switches between perfect x -alignments with the large and the middle principal axis (d).

Leading corrections in the ratios of the sphere radius to intra-object distances are contained within the Oseen approximation, yielding

$$\mathbf{H}_{i,j}^{\text{Oseen}} = \mathbf{H}_{i,j}^{\text{Stokes}} + \frac{1 - \delta_{i,j}}{8\pi\eta r_{i,j}} \left[\mathbb{1} + \frac{\mathbf{r}_{i,j}\mathbf{r}_{i,j}}{r_{i,j}^2} \right]. \quad (25)$$

Finally, we compared the Stokes and Oseen results with those following from the full Rotne–Prager tensor (6). Since we found only minor differences between the outcomes of the Oseen and the Rotne–Prager treatments (see figure 5(a)), we only present the results of the comparison between the Stokes and the Rotne–Prager results. It is interesting to note that

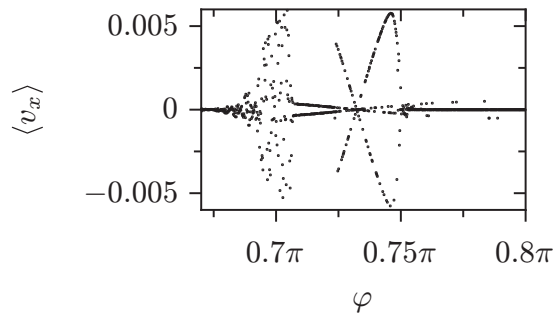


Figure 13. Average velocities in the x -direction for 2000 randomly rotated initial conditions taken along the achiral curve $(h/\rho)_1$ given by equation (22) are displayed for $\rho = 5$ and $\varphi \in [0.67\pi, 0.8\pi]$ in steps of $\Delta\varphi = 1.65 \times 10^{-4}\pi$. The equations of motion (11) were numerically solved with these initial conditions up to time $t = 8000$ and the average $\langle v_x \rangle$ was estimated by means of equation (20) for $t_0 = 7000$, $\tau = 1$ and $N = 1000$. Apart from the region $\varphi \in (0.68\pi, 0.7066\pi)$ where the average velocities seemingly are random, they form up to four branches. Coming in pairs of opposite average velocities they maintain the achiral symmetry at each point along the achiral curve. In a part of the achiral curve with $\varphi \in [0.8\pi, \pi]$, which is not shown, the lateral average velocity forms a single branch with $\langle v_x \rangle = 0$ within numerical precision.

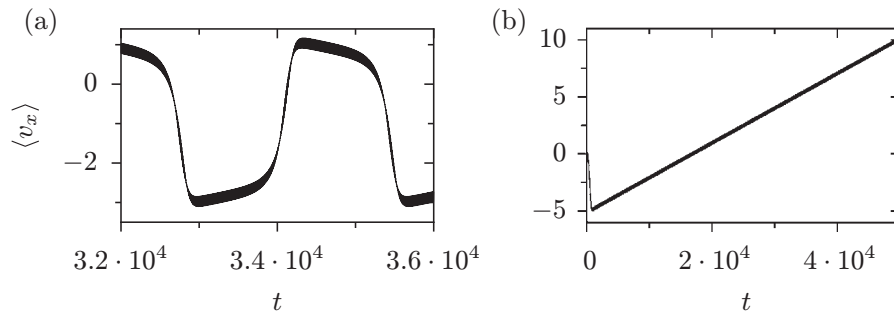


Figure 14. The center of mass motion on the achiral curve, equation (22), (a) for $\varphi = 0.7\pi$ and (b) $\varphi = 0.71092\pi$, both for $\rho = 5$. The long period $T \approx 2730$ in panel (a) leads to under-sampling of the average $\langle v_x \rangle$ displayed in figure 13 and, as a consequence, to the cloud of random points in the screw angle region between 0.66π and 0.7066π . In contrast, the case in panel (b) approaches uniform motion in the positive x -direction after a short transient.

the rotational motion and the internal motion of the object are qualitatively quite similar for the Stokes and the Rotne–Prager treatments. Figure 15 illustrates the qualitative agreement of the two approximations by comparing the alignment of (a) the middle principal axis with the instantaneous rotation axis and (b) the x -component of the instantaneous rotation axis.

Also the deformational motion of the object is quite similar see figure 16 displaying a comparison of the magnitudes of the principal axes and the relative volume for the two approximations. Hence the rotational and internal motions of an object are mainly determined by the action of the Stokes forces.

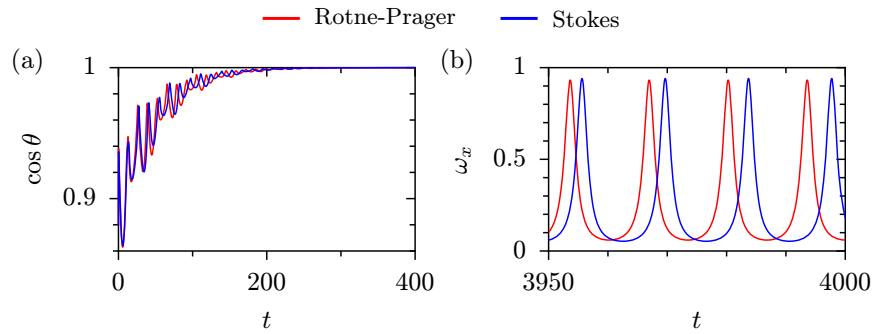


Figure 15. A comparison of the rotational motion of an object under the sole action of the Stokes forces (blue) and the full Rotne–Prager tensor (red) is presented for a spiral object with $\varphi = 0.87$, $h/\rho = 0.2073$ and $\rho = 7$ with an initial orientation that leads to the uppermost velocity branch (see figure 5(a)) within the Rotne–Prager treatment. Panel (a) displays the approach of the angle between the instantaneous rotation axis and the middle principal axis, showing good agreement between the Stokes and the Rotne–Prager treatment. (b) The oscillations of the x -component of the instantaneous rotation axis follow the same pattern with the same amplitude and slightly smaller period under the influence of the Rotne–Prager mobility as in the case of the Stokes forces.

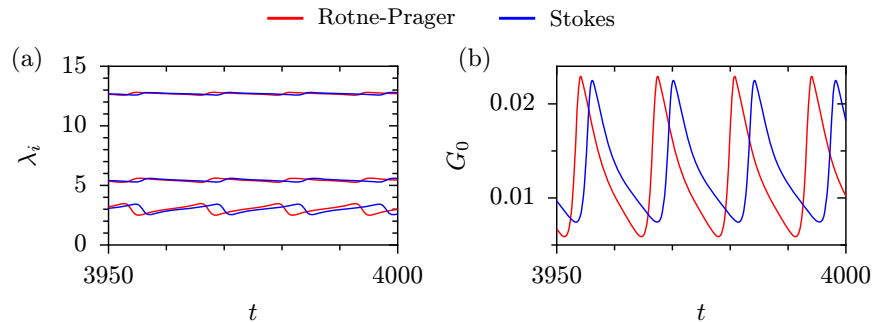


Figure 16. For the parameter values detailed in figure 15, the hydrodynamic interactions contained in the full Rotne–Prager mobility tensor (red) have little influence on the magnitudes of the principal axes displayed in panel (a) compared to the sole action of the Stokes forces (blue). Also the chirality index presented in panel (b) differs in a small shift of the period, which is slightly shorter, and in the amplitude, which is larger in the case of the Rotne–Prager treatment.

In the present case of uniform shear flow the sole action of the Stokes forces cannot lead to a translational motion in the vorticity direction. This rigorously follows from the fact that the internal forces exerted by the FENE-Fraenkel springs do not contribute to the motion of the center of mass for a uniform shear flow within the Stokes approximation, $\sum_{i,j} \mathbf{H}_{i,j}^{\text{Stokes}} \mathbf{F}_j = 0$, and hence the center of mass motion is determined by

$$\dot{\mathbf{X}} = \frac{1}{4} \sum_n \mathbf{v}(\mathbf{x}_n). \quad (26)$$

Therefore, in a uniform shear flow, as given by equation (10), the center of mass cannot move perpendicularly to the flow direction within the Stokes approximation and the lateral drift consequently vanishes. Only the small, non-diagonal terms of the mobility tensor implied by both the Oseen and the Rotne–Prager treatments lead to a coupling between the translational and the rotational motion and, in this way, facilitate a center of mass motion perpendicular to the flow direction. For more complicated flow fields with non-uniform vorticity, such a coupling becomes possible and may lead to chiral separation even within the Stokes approximation [1].

5. Conclusions

We presented a case study of the dynamics of deformable chiral objects consisting of four spheres in a uniform shear flow. Internal forces due to relative position changes of the spheres were modeled by FENE-Fraenkel forces such that the bond lengths may only vary within a prescribed range. In the equilibrium configuration, the internal forces balance each other. Forces exerted by the fluid on the object drive the object out of this equilibrium state. Due to the small size and mass of the spheres, inertia terms in the equations of motion could be neglected and a purely overdamped motion was studied. The influence of the flowing fluid on the objects was described by means of the Rotne–Prager mobility tensor; this tensor includes the Stokes force and hydrodynamic interactions (up to second order in the sphere radius to the intra-object distance ratio) between the spheres constituting an object. If only the Stokes forces are considered and hydrodynamic interactions are neglected, then, in a uniform shear flow, the object moves with its center of mass strictly in the direction of the flow field. Moreover, it also performs a rotational motion about the center of mass with an instantaneous rotation axis pointing in the direction of vorticity. However, the hydrodynamic interactions cause a coupling between the translational and the rotational motion of the object. These interactions let the rotating object act as a propeller which drives the object transversely to the flow field in or against the direction of its vorticity. The direction of this component of motion is opposite for an object and its mirror images, thus leading to different transport properties of enantiomers.

In general, one finds different asymptotic forms of motion for objects with the same equilibrium configuration. These motional states correspond to different attractors of the equations of motion. They can be distinguished by the magnitude of their average velocities in the vorticity direction and the orientation of the object relative to the instantaneous rotation axis which typically points in the vorticity direction. The maximum number of attractors that we identified in the present study was four; this corresponds to (i) two alignments of the instantaneous axis of rotation with the large and the small principal axes and (ii) two alignments with the middle axis. We documented the typical translational, rotational and deformational motions in detail with the example of an object with a particular equilibrium configuration. The same qualitative motion patterns were observed for numerous other equilibrium configurations but are not presented here.

The reason why we studied deformable rather than rigid objects was not only to obtain a more realistic modeling but also because the numerical implementation of the constraints defining rigid objects in three dimensions is more difficult than allowing for deformations. Moreover, we found that the flexibility of the objects may lead to dynamical symmetry breaking for objects with achiral equilibrium configurations. We demonstrated that the deformations of achiral objects may lead to chiral configurations with a finite chirality index G_0 accompanied by a finite average lateral velocity in or opposite to the vorticity direction. If the initial conditions

are sampled from a symmetric distribution, containing mirror-symmetry-related orientations with equal weight, then motional states with opposite chirality emerge with equal probability. In this way, the mirror symmetry of the total state space is recovered.

The effects of chirality on the transport properties are relatively weak in the present case of a uniform shear flow. This finding is also in agreement with the results of [17] for bond-strength-induced chirality. The situation however is expected to drastically change for non-uniform shear flows, which already induce a coupling between translational and rotational motion within the Stokes approximation. It is plausible to assume that there, locally, the same principal mechanisms are still at work: the local vorticity leads to a rotation of the object, which then acts via hydrodynamic interactions as a propeller pushing itself in or opposite to the direction of the instantaneous rotation axis depending on its chirality. In non-uniform shear flows, objects of different chirality, however, will be moved to different regions of the flow field where they then are advected with different velocities. This effect can significantly enhance the influence of the chirality on transport properties and, hence, may form the basis of effective, purely physical enantiomer-separation mechanisms. Promising experimental candidates are surface acoustic wave-driven vortex flows in fluids confined to micro-chambers [29, 30] or flows through micro- or nanofluidic channels [31].

Before such practical applications can be envisaged, however, the so far neglected influences of thermal noise, hydrodynamic interactions between different objects of the same and different chiralities, as well as between objects and walls confining the fluid should all be taken into account and investigated.

Acknowledgments

We express our sincere thanks to Marcin Kostur and Juyeon Yi for valuable discussions. This project was supported by the Deutsche Forschungsgemeinschaft, grant number HA-1517/28-1.

Appendix. Achiral configurations

By the construction of the spiral objects, the length $d_{n,m}$ of the edge connecting the n th with the m th sphere only depends on the absolute value of the difference between n and m , $d_{n,m} = l(|n - m|)$. In the general case, a spiral object hence has three equal edges of length $l(1)$, two of length $l(2)$ and one of length $l(3)$, where

$$l(n) = [2\rho^2(1 - \cos(n\varphi)) + n^2 h^2]^{1/2}. \quad (\text{A.1})$$

One branch of achiral configurations possesses two equilateral and two isosceles faces; see figure 3(c). They have five equally long edges with $l(1) = l(2)$. This condition determines the relative rise as a function of the screw angle to be

$$(h/\rho)_1^2 = \frac{2}{3}(\cos(2\varphi) - \cos(\varphi)), \quad (\text{A.2})$$

where the screw angle is restricted to $2\pi/3 < \varphi < 4\pi/3$ in order that the right-hand side stays positive. On this curve the maximal value of the relative rise is reached at $\varphi = \pi$ and there takes the value $h/\rho = 2/\sqrt{3}$.

Achiral configurations with four identical isosceles faces result from the requirement $l(1) = l(3)$. The relative rise as a function of the screw angle then becomes

$$(h/\rho)_2^2 = \frac{1}{4}(\cos(3\varphi) - \cos(\varphi)), \quad (\text{A.3})$$

with $\pi/2 < \varphi < 3\pi/2$. This function vanishes at $\varphi = \pi$ as well as at the borders of the indicated interval, and has a maximum at $\varphi \approx 0.696\pi$, $h/\rho \approx 0.620$.

The two achiral branches cross at the special angle at which $\cos \varphi = -2/3$, yielding $h/\rho = \sqrt{10/27}$, where all three edge lengths agree with each other, resulting in a regular tetrahedron.

References

- [1] Kostur M, Schindler M, Talkner P and Hänggi P 2006 *Phys. Rev. Lett.* **96** 014502
- [2] Hänggi P and Marchesoni F 2009 *Rev. Mod. Phys.* **81** 387
- [3] Crusats J, El-Hachemi Z and Ribó J M 2010 *Chem. Soc. Rev.* **39** 569
- [4] Howard D W, Lightfoot E N and Hirschfelder J O 1976 *AIChE J.* **22** 794
- [5] de Gennes P G 1999 *Europhys. Lett.* **46** 827
- [6] Brenner H 1964 *Chem. Eng. Sci.* **19** 631
- [7] Chen P and Chao C H 2007 *Phys. Fluids* **19** 017108
- [8] Makino M, Arai L and Doi M 2008 *J. Phys. Soc. Japan* **77** 064404
- [9] Marcos Fu H C, Powers T R and Stocker R 2009 *Phys. Rev. Lett.* **102** 158103
- [10] Grzybowski B A and Whitesides G M 2002 *Science* **296** 718
- [11] Ghosh A and Fischer P 2009 *Nano Lett.* **9** 2243
- [12] D'Urso A, Randazzo R, Lo Faro L and Purrello R 2010 *Angew. Chem. Int. Edn Engl.* **49** 108
- [13] Doi M and Makino M 2005 *Phys. Fluids* **17** 043601
- [14] Makino M and Doi M 2005 *Phys. Fluids* **17** 103605
- [15] Eichhorn R 2010 *Phys. Rev. Lett.* **105** 034502
- [16] Eichhorn R 2010 *Chem. Phys.* **375** 568
- [17] Watari N and Larson R G 2009 *Phys. Rev. Lett.* **102** 246001
- [18] Hsieh C C, Jain S and Larson R G 2006 *J. Chem. Phys.* **124** 044911
- [19] Purcell E M 1977 *Am. J. Phys.* **45** 3
- [20] Rotne J and Prager S 1969 *J. Chem. Phys.* **50** 4831
- [21] Dhont J K G 1996 *An Introduction to Dynamics of Colloids* (Amsterdam: Elsevier)
- [22] Radhakrishnan K and Hindmarsh A C 1993 *LLNL Report UCRL-ID-113855*
- [23] Petzold L 1983 *SIAM J. Sci. Stat. Comput.* **4** 136
- [24] Jones E *et al* 2001 *SciPy: Open source scientific tools for Python* <http://scipy.org/>
- [25] Solymosi M, Low R J, Grayson M and Neal M P 2002 *J. Chem. Phys.* **116** 9875
- [26] Harris A B, Kamien R D and Lubensky T C 1999 *Rev. Mod. Phys.* **71** 1745
- [27] Miles R E 1965 *Biometrika* **52** 636
- [28] Reimann P and Hänggi P 2002 *Appl. Phys. A* **75** 169
- [29] Guttenberg Z, Rathgeber A, Keller S, Rädler J O, Wixforth A, Kostur M, Schindler M and Talkner P 2004 *Phys. Rev. E* **70** 056311
- [30] Frommelt T, Kostur M, Wenzel-Schäfer M, Talkner P, Hänggi P and Wixforth A 2008 *Phys. Rev. Lett.* **100** 034502
- [31] Meinhardt S, Smiatek J, Eichhorn R and Schmid F 2012 *Phys. Rev. Lett.* **108** 214504